Available online at www.sciencedirect.com
SCIENCE DIRECT®
International Journal of Heat and Mass Transfer 47 (2004) 4625–4635
International Journal of HEAT and MASS TRANSFER
www.elsevier.com/locate/ijhmt

Modeling of soot particles growth in fuel-rich premixed flame

Masaaki Okuyama [a,*], Ryozo Echigo [b], Katsunori Hanamura [c], Hideo Yoshida [d], Motoi Koda [e], Tomomi Koganezawa [f]

[a] Department of Mechanical Engineering, Yamagata University, Yonezawa, Yamagata, 992-8510, Japan
[b] Department of Mechanical Engineering, Shibaura Institute of Technology, Minato-ku, Tokyo, 108-8548, Japan
[c] Research Center for Carbon Recycling and Energy, Tokyo Institute of Technology, Meguro-ku, Tokyo, 152-8552, Japan
[d] Department of Mechanical Engineering, Kyoto University, Sakyo-ku, Kyoto, 606-8501, Japan
[e] Department of Mechanical and Control Engineering, Tokyo Institute of Technology, Meguro-ku, Tokyo, 152-8550, Japan
[f] Power and Industrial Systems R&D Laboratory, Hitachi Ltd., Hitachi-naka, Ibaraki, 312-0034, Japan

Received 6 May 2003; received in revised form 1 August 2003
Available online 26 June 2004

Abstract

The soot formation process and the structure of a fuel-rich premixed flame stabilized in the downstream side of a porous medium have been investigated by experimental measurements and numerical analysis. In the numerical analysis, a modified Tesner's model for the reaction rate of soot formation has been introduced through a comparison between measured and calculated distributions of the temperature and the species mole fractions. Furthermore, a novel model for soot growth is developed, taking both surface and coalescence growths into account. On the basis of this model, the following results are obtained. Surface growth becomes dominant immediately after the beginning of soot formation. In the downstream side, the soot particle increases due to grow by the coalescence with smaller soot particles, and decrease as a result of collision with radicals and coalescence with larger soot particles.

Keywords: Premixed flame; Radiation controlled flame; Soot formation; Coagulation; Growth process of soot; Statistical and geometrical model

1. Introduction

The authors are interested in the control of soot formation in luminous flames of hydrocarbon fuels from two utterly different stand points. One point is, of course, the suppression of soot emission in conventional combustion. The other is the enhancement of soot formation in the "carbon solidification combustion" concept suggested previously as a countermeasure to global warming by the authors [1]. In a carbon solidification combustion system, the energy of hydrocarbon fuels is extracted mainly from the reaction of hydrogen, while part of the carbon is solidified as soot; therefore, if the solidified soot can be effectively separated from the combustion products, the exhausted gas consists of a relatively high concentration of H_2O and reduced CO_2. For both of the approaches mentioned above, a precise knowledge of the processes of soot formation and growth as well as PAH formation is necessary.

The soot growth model studied previously is classified into two categories, i.e., surface growth and coagulation growth. For the surface growth, the first-order kinetics law was employed by Haynes et al. [2] and the surface reaction model was introduced by Mauss et al. [3]. For the coagulation growth, Smoluchowski's model was adopted by Lai et al. [4].

The aforementioned carbon solidification combustion process [1] was developed during a series of studies

* Corresponding author. Tel./fax: +81-238-26-3257.
E-mail address: tg017@yz.yamagata-u.ac.jp (M. Okuyama).

0017-9310/$ - see front matter © 2004 Elsevier Ltd. All rights reserved.
doi:10.1016/j.ijheatmasstransfer.2003.10.044

Nomenclature

a	frequency factor for soot formation (s^{-1})
A	frequency factor for exothermic reaction (s^{-1}) or endothermic reaction (1/kg/s)
A_c	frequency factor for radical oxidation (m^3/kg/s)
A_p	surface area of an equivalent particle of porous medium (m^2)
b	frequency factor for radical destruction (m^3/s)
C	specific heat of porous medium (J/kg/K)
C_0	frequency factor for collision between soot particles and radicals (m^3/s)
C_2	the second Planck's constant (1.4388×10^{-2} mK)
C_r	dimensionless coefficient, Eq. (24)
c_p	specific heat of gas phase at constant pressure (J/kg/K)
D	diffusion coefficient (m^2/s)
d_p	mean diameter of a soot particle (m)
E	activation energy (J/mol)
E_n	exponential integral function of the nth order, Eq. (20)
$\overline{f(n,k)}$	function defined by Eq. (23)
f	frequency factor for radical branching reaction (s^{-1})
$f_v(r,x)$	local soot volume function (m^{-1})
$f_{v,r}(r,x)$	accumulated soot volume function
$f_{v,s}(x)$	total soot volume function, Eq. (22)
g	frequency factor for radical terminating reaction (s^{-1})
g_0	frequency factor for radical destruction (m^3/s)
h	heat of reaction (J/kg)
h_p	heat transfer coefficient around an equivalence particle of porous medium ($W/m^2/K$)
I_b	total emissive power of a black body (W/m^2)
I_0, I_e	incident radiance (W/m^2)
l	dimensionless soot particle coalescence region (m)
M_R	molar mass of radical (kg/mol)
m	exponent in Eq. (24)
N_A	Avogadro's number [$=6.02\times10^{23}\,mol^{-1}$]
$N_s(x)$	soot number density, Eq. (27) (m^{-3})
n	real part of complex refractive index of soot particles
nk	complex part of complex refractive index of soot particles
n_p	number density of equivalent particles of porous medium (m^{-3})
n_R	radical number density (m^{-3})
q_r^+, q_r^-, q_r	radiative heat fluxes in positive and negative directions and net radiative heat flux, respectively (W/m^2)
R	gas constant [$=8.134$ J/mol/K]
Re	Reynolds number
R_{min}	initial soot particle radius (m)
R_∞	maximum soot particle radius (m)
r	soot particle radius (m)
$r'_a(r,x)$	growth rate of soot particle radius (m/s)
$r_{ave}(x)$	mean soot particle radius (m)
$r'_e(r,x)$	surface growth rate of soot particle radius (m/s)
$r_E(r,x)$	equivalent radius defined by Eq. (5) (m)
r_m	radius increment (m)
$s'_a(r,x)$	growth rate of soot particle surface area (m^2/s)
$s'_e(r,x)$	surface growth rate of soot particle surface area (m^2/s)
T	temperature (K)
T_0	initial temperature of mixture (K)
t	time (s)
u	velocity of mixture (m/s)
W	reaction rate (kg/m^3/s)
X	dimensionless coordinate system
x	geometrical coordinate system (m)
Y	mole fraction of species

Greek symbols

κ	absorption coefficient (m^{-1})
λ	thermal conductivity (W/m/K)
μ	cosine
ν	kinematic viscosity (m^2/s)
ρ	gas density (kg/m^3)
σ	Stefan–Boltzmann constant ($=56.7\times10^{-9}$ $W/m^2/K^4$)
τ	optical coordinate system
τ_p	optical thickness of porous medium
ϕ	equivalence ratio

Subscripts

en	endothermic reaction
ex	exothermic reaction
fuel	fuel
g	gas
nitro	nitrogen
oxy	oxygen
p	porous medium
pro	products
soot	soot

on combustion enhancement using porous media over a period of more than 15 years [5,6]. In recent experiments relating to carbon solidification combustion [1,7,8] a *luminous* flame was successfully formed at the down-

stream side of a porous medium for CH_4–air premixed combustion. The structure of this *luminous* flame was also investigated theoretically by means of a numerical calculation [9]; since the modified Tesner's model [10] used for soot formation was incorporated with the assumption that the diameter of soot particles is constant, only their number density increases. Although this analysis detail the important features of the luminous flame, the calculated soot number density profile does not correspond to the actual one in the soot inception region where both soot particle radius and soot number density vary rapidly [11].

Therefore, the purpose of this study is to clarify the growth process of soot particles while taking the surface and coalescence growth into account. In particular, the sophisticated model developed for the dropwise condensation phenomena by Tanaka [12] is applied to the present soot growth, assuming a similarity between the two phenomena. Although actual soot particles grow according to a chain structure as reported in Ref. [13], the present model is considered to demonstrate qualitatively correct features, because the coalescence probability is statistically evaluated for polydispersed soot particles. In this work, to support the numerical analysis of the flame structure with taking into account the growth process of soot particles, the parameters used in the calculation were basically derived from the experimental values.

2. Experimental detail

Fig. 1 shows a schematic of the combustor [1]. Two porous media made of ceramics were installed in a quartz tube (i.d. 100 mm) to form a combustion chamber; porous medium I (normal mesh length 1/30) was 50 mm thickness and porous medium II (normal mesh length 1/30) was 25 mm thickness. A methane–air mixture was supplied from the bottom of the quartz tube, and the one-dimensional flame was stabilized between the two porous media.

A chromel–alumel thermocouple with diameter of 0.1 mm was used for the measurement of the gas temperature in the combustion chamber. In this case, along the flow direction the thermocouple was scanned sufficiently quickly to remain free from the effect of soot deposition on its surface. The gas temperature was estimated from the measured temperature on the basis of the corrections for radiative heat losses and the time constant of the thermocouple [1].

On-line gas chromatography with thermal conductivity and flame ionization detectors was used for the analysis of light hydrocarbons. Identification of species was accomplished by matching the GC retention times to pure components as well as the mass spectral fragmentation patterns to MS libraries.

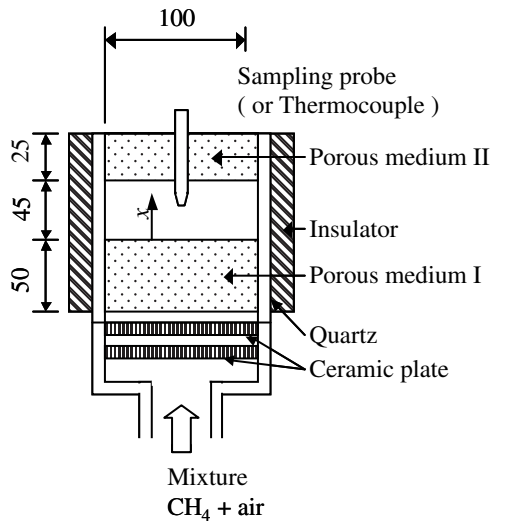

Fig. 1. Schematic diagram of radiation-controlled combustor. Dimensions in mm.

3. Theoretical analysis

3.1. Analytical model

Fig. 2 shows a one-dimensional analytical model for a fuel-rich premixed flame. A methane–air mixture at an initial temperature, T_0, flows into the porous medium at $x = -x_p$, while the combustion gas and soot particles flow out at $x = x_e$. From the viewpoint of soot volume or soot number density, the phenomena of the soot growth process are considered to be similar to those of dropwise condensation. Hence, the soot growth due to coalescence is assumed to be described in a manner similar to Tanaka's dropwise condensation model [12], and the surface growth process is also taken into account. It is assumed that stoichiometric amounts of the fuel and required oxygen are consumed in the exothermic reaction to produce a maximum temperature, and then, the endothermic reaction occurs for the soot formation. The other assumptions are similar to those of previous works [9,14].

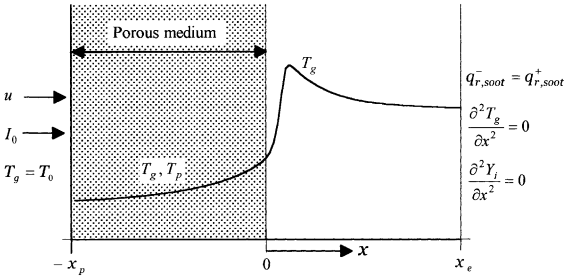

Fig. 2. Analytical model.

3.2. Reaction model

The exothermic reaction rate, W_{ex}, is described by an irreversible first-order isomerization, i.e., fuel + oxygen → product, as follows:

$$W_{ex} = A_{ex}\rho_g Y_{fuel}^{\delta} Y_{oxy}^{1-\delta} \exp\left(-\frac{E_{ex}}{RT_g}\right), \quad (1)$$

where $\delta = 1$ for $\phi < 1$, while $\delta = 0$ for $\phi \geqslant 1$.

The endothermic reaction for soot formation, W_{en}, is based on Tesner's model [10]. The formation rate of the radical number density, n_R, is expressed as

$$\frac{dn_R}{dt} = u\frac{dn_R}{dx} = A_{en}\rho_g Y_{fuel} \exp\left(-\frac{E_{en}}{RT_g}\right) + (f-g)n_R - g_0 n_R \times \int_{R_{min}}^{R_\infty} N(p,x)\,dp - A_c\rho_g Y_{oxy} n_R. \quad (2)$$

Here, the first, second, third and fourth terms on the right-hand side denote production, branching and destruction, termination by collision with the soot particles, and oxidation, respectively. Thus, Tesner's model is modified by adding the oxidation term in order to suppress soot formation in the exothermic reaction zone. The soot formation rate, W_{en}, is expressed as

$$W_{en} = \frac{\pi}{6}\rho_{soot} n_R \int_{R_{min}}^{R_\infty} (2p)^3 (a\delta_r - bN(p,x))\,dp, \quad (3)$$

where $\delta_r = 1$ for the initial soot particle radius (R_{min}), while $\delta_r = 0$ for $r > R_{min}$.

3.3. Soot growth model

Soot particles are assumed to be generated from radicals produced according to Eq. (2), and are assumed to grow by surface and coalescence growth. At time $t = dx/u$ from the start of soot formation, $N_s(r,x)dr$ soot particles per unit volume having radii in the interval $(r, r+dr)$ exist. The radii of these soot particles increase at a mean rate $r'_a(r,x)$ by both coalescence and surface growth. A previous soot growth model, i.e., Smoluchowski's model, is modeled in the free molecular regime and according to this model, soot is assumed to grow by collision with particles. In this study, the coalescence of soot particles is modeled by the coalescence probability which is statistically evaluated for polydispersed soot particles. Although the present analysis has been performed using a three-dimensional model, the following figures are shown in two-dimensional form. As shown in Fig. 3(a), we consider the case of the coalescence of soot particles with radius η and those with radius $r(\eta > r)$; if

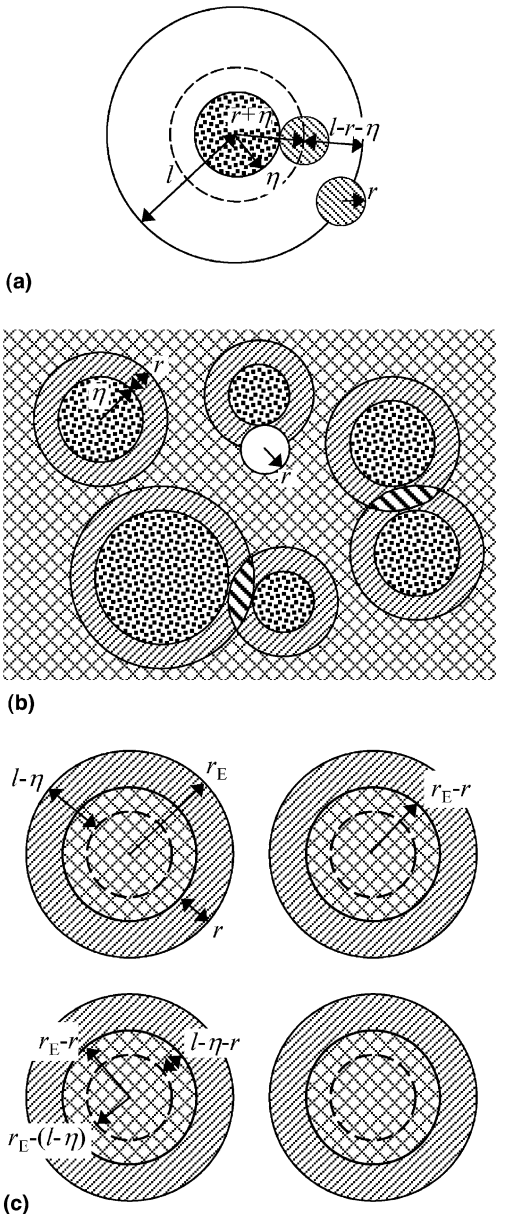

Fig. 3. (a) Soot particles coalescence model. (b) Configuration of soot particles with radii larger than r. (c) Corrected configuration of soot particles.

the centers of soot particles with radius r exist in the coalescence region which is the spherical space between radius η and radius l, small soot particles having radii in the interval $(r, r+dr)$ will coalescence. Consequently, they become extinct by collision with, or due to the generation of interparticular force with, large soot particles having radii in the interval $(\eta, \eta+d\eta)$. The main assumptions for the soot growth model are as follows:

(1) Soot particles are spherical, and the calculation of the soot formation and growth process is performed three-dimensionally in a unit volume.
(2) In the open space where soot particles can be distributed, they are uniformly distributed in the order of particle size.
(3) In the case of coalescence between two soot particles of different sizes, the larger one grows, while the smaller one becomes extinct.
(4) The surface growth of soot particles is due to the collision of radicals with a soot particle.

Fig. 3(b) illustrates the configuration of soot particles whose radii are larger than r.

The hatched–crosshatched region having a volume of

$$1-\int_r^{R_\infty}\frac{4}{3}\pi p^3 N(p,x)\,\mathrm{d}p \tag{4}$$

is the open space in which soot particles whose radii are equal to or smaller than r can be distributed. Moreover, the centers of soot particles with radius r have to be located within the crosshatched region. Next, the concept of a hydraulic diameter $r_{\mathrm{E}}(r,x)$ is introduced; the hatched–crosshatched region in Fig. 3(b) is replaced by the hatched–crosshatched layers in Fig. 3(c), such that the ratio of surface area remains unchanged. Hence, the radius $r_{\mathrm{E}}(r,x)$ is given as

$$r_{\mathrm{E}}(r,x)=3\frac{1-\int_r^{R_\infty}\frac{4}{3}\pi p^3 N(p,x)\,\mathrm{d}p}{\int_r^{R_\infty}4\pi p^2 N(p,x)\,\mathrm{d}p}. \tag{5}$$

As a result, the centers of soot particles with the radius r have to be located within the crosshatched region in Fig. 3(c). Thus, the probability of the soot particles with radii in the interval $(r,r+\mathrm{d}r)$ in the crosshatched region where those soot particles can actually reside is estimated as

$$\frac{N(r,x)\,\mathrm{d}r}{\left(1-\frac{r}{r_{\mathrm{E}}(r,x)}\right)^3\left(1-\int_r^{R_\infty}\frac{4}{3}\pi p^3 N(p,x)\,\mathrm{d}p\right)}. \tag{6}$$

We shall show that the following expression represents the number of small soot particles per unit volume having radii in the interval $(r,r+\mathrm{d}r)$ which become extinct by coalescence with large soot particles having radii in the interval $(\eta,\eta+\mathrm{d}\eta)$.

$$\frac{4\pi}{3}\left\{[r_{\mathrm{E}}(r,x)-r]^3-[r_{\mathrm{E}}(r,x)-l+\eta]^3\right\}\times\frac{\eta^2 N(\eta,x)\,\mathrm{d}\eta}{(r_{\mathrm{E}}(r,x)-r)^2}\psi(r,x)N(r,x)\,\mathrm{d}r \tag{7}$$

where

$$\psi(r,x)=\frac{1}{\left(1-\int_r^{R_\infty}\frac{4}{3}\pi p^3 N(p,x)\,\mathrm{d}p\right)\left(1-\frac{r}{r_{\mathrm{E}}(r,x)}\right)}. \tag{8}$$

Since the integral region for η is $r<\eta\leqslant R_\infty$, the extinct soot number density for soot particles with radius r as a result of coalescence is

$$\frac{4\pi}{3\left(\frac{\mathrm{d}x}{u}\right)(r_{\mathrm{E}}(r,x)-r)^2}N(r,x)\psi(r,x)\,\mathrm{d}r\int_r^{R_\infty}\left\{[r_{\mathrm{E}}(r,x)-r]^3-[r_{\mathrm{E}}(r,x)-l+\eta]^3\right\}\eta^2 N(\eta,x)\,\mathrm{d}\eta. \tag{9}$$

The balance of soot number density, $N(r,x)$, having radius r is expressed as

$$\begin{aligned}\frac{\partial N(r,t)}{\partial t}&=u\frac{\partial N(r,x)}{\partial x} && \text{(I)}\\ &=\frac{1}{\partial r}[a\delta_r-bN(r,x)\,\mathrm{d}r]n_{\mathrm{R}} && \text{(II)}\\ &\quad-\frac{\partial(N(r,x)r'_a(r))}{\partial r} && \text{(III)}\\ &\quad-\frac{4\pi N(r,x)\psi(r,x)}{3\left(\frac{\mathrm{d}x}{u}\right)(r_{\mathrm{E}}(r,x)-r)^2}\\ &\quad\times\int_r^{R_\infty}\left\{[r_{\mathrm{E}}(r,x)-r]^3-[r_{\mathrm{E}}(r,x)-l+\eta]^3\right\}\\ &\quad\times\eta^2 N(\eta,x)\,\mathrm{d}\eta.10 && \text{(IV)}\end{aligned} \tag{10}$$

(term I: Convection)
(term II: Formation and termination by collision with radicals)
(term III: Growth by coalescence)
(term IV: Termination by coalescence with larger particles)

The growth rate $r'_a(r,x)$ of soot particles having radius r is

$$4\pi r^2 N(r,x)\,\mathrm{d}r[r'_a(r,x)-r'_e(r,x)]\frac{\mathrm{d}x}{u}=\int_{R_{\min}}^{r}\frac{4\pi}{3}r^2\left\{[r_{\mathrm{E}}(\eta,x)-\eta]^3-[r_{\mathrm{E}}(\eta,x)-l+r]^3\right\}\times\frac{N(\eta,x)N(r,x)}{(r_{\mathrm{E}}(\eta,x)-\eta)^2}\psi(\eta,x)\frac{4\pi}{3}\eta^3\,\mathrm{d}r\,\mathrm{d}\eta, \tag{11}$$

where the left-hand side of Eq. (11) represents the increase in the volume of soot particles having radius r due to coalescence with small soot particles having radius $\eta(\eta<r)$. The right-hand side of Eq. (11) represents the

decrease in the volume of small soot particles due to coalescence with soot particles having radius r.

The surface growth rate, $r'_e(r,x)$, of soot particles having radius r is

$$4\pi r^2 N(r,x)\,\mathrm{d}r r'_e(r,x)\frac{\mathrm{d}x}{u} = C_0 n_\mathrm{R} N(r,x)\,\mathrm{d}r\frac{M_\mathrm{R}}{N_\mathrm{A}\rho_\mathrm{R}}\frac{\mathrm{d}x}{u}, \tag{12}$$

where the left-hand side of Eq. (12) represents the increase in the volume of soot particles having radius r due to surface growth. The right-hand side of Eq. (12) represents the decrease in the volume of radicals due to collision with soot particles having radius r.

3.4. Basic equations

Using the preceding assumptions, the time-dependent energy equations for both gas and particulate phases as well as the continuity equation for species are formulated, respectively, as $(-x_p \leqslant x < 0)$

$$\rho_\mathrm{g}\frac{\partial Y_i}{\partial t} + \rho_\mathrm{g} u\frac{\partial Y_i}{\partial x} = \rho_\mathrm{g} D\frac{\partial^2 Y_i}{\partial x^2} + \sum_j W_j \tag{13}$$

$$\rho_\mathrm{g} c_p\frac{\partial T_\mathrm{g}}{\partial t} + \rho_\mathrm{g} c_p u\frac{\partial T_\mathrm{g}}{\partial x} = \lambda_\mathrm{g}\frac{\partial^2 T_\mathrm{g}}{\partial x^2} + \sum_j h_j W_j - h_\mathrm{p} n_\mathrm{p} A_\mathrm{p}(T_\mathrm{g} - T_\mathrm{p}) \tag{14}$$

$$\rho_\mathrm{p} C\frac{\partial T_\mathrm{p}}{\partial t} = \lambda_\mathrm{p}\frac{\partial^2 T_\mathrm{p}}{\partial x^2} - \frac{\partial q_{r,p}}{\partial x} + h_\mathrm{p} n_\mathrm{p} A_\mathrm{p}(T_\mathrm{g} - T_\mathrm{p}) \quad (0 \leqslant x \leqslant x_e) \tag{15}$$

$$\rho_\mathrm{g}\frac{\partial Y_i}{\partial t} + \rho_\mathrm{g} u\frac{\partial Y_i}{\partial x} = \rho_\mathrm{g} D\frac{\partial^2 Y_i}{\partial x^2} + \sum_j W_j \tag{16}$$

$$\rho_\mathrm{g} c_p\frac{\partial T_\mathrm{g}}{\partial t} + \rho_\mathrm{g} c_p u\frac{\partial T_\mathrm{g}}{\partial x} = \lambda_\mathrm{g}\frac{\partial^2 T_\mathrm{g}}{\partial x^2} + \sum_j h_j W_j - \frac{\partial q_{r,\mathrm{soot}}}{\partial x}. \tag{17}$$

Here, $i =$ fuel, oxygen, nitrogen, products and soot, $j =$ ex (exothermic reaction rate), and $j =$ en (endothermic reaction rate).

The radiation fluxes from the porous medium and soot particles are integrated in order to evaluate the divergence of radiation as

$$\frac{\partial q_{r,k}(\tau_k)}{\partial x} = -2\pi\kappa_k\left\{I_{0,k}E_2(\tau_k). + I_{e,k}E_2(\tau_{e,k}-\tau_k) - 2I_{b,k}(\tau_k) + \int_0^{\tau_{e,k}} I_{b,l}(\tau'_k)E_1(|\,\tau_k - \tau'_k\,|)\,\mathrm{d}\tau'_k\right\}, \tag{18}$$

where $k =$ p and $l =$ p in Eq. (18) are for the porous medium, while $k =$ soot and $l =$ gas are for the soot particles. Furthermore, $I_b(\tau)$ and $E_n(\tau)$ are expressed respectively as

$$I_{b,l}(\tau) = \frac{\sigma T_l^4}{\pi} \tag{19}$$

$$E_n(\tau_k) = \int_0^1 \mu^{n-2}\exp\left(-\frac{\tau_k}{\mu}\right)\mathrm{d}\mu. \tag{20}$$

The absorption coefficient $\kappa_\mathrm{soot}(x)$ of soot particles is [15]

$$\kappa_\mathrm{soot}(x) = 3.6\left\{36\pi f_{v,s}(x)\frac{\overline{f(n,k)}T_\mathrm{g}(x)}{C_2}\right\} \tag{21}$$

$$f_{v,s}(x) = \frac{\pi}{6}\int_{R_\mathrm{min}}^{R_\infty}(2p)^3 N(p,x)\,\mathrm{d}p \tag{22}$$

$$\overline{f(n,k)} = \frac{n^2 k}{\{n^2 + (nk)^2 + 2\}^2 + 4n^2k^2}. \tag{23}$$

The soot radius increment r_m is

$$r_m = \frac{d_\mathrm{p}}{2}(C_r)^{m-1}, \tag{24}$$

where the complex refractive index is $n - ink = 1.57 - 0.56\mathrm{i}$ [16].

The boundary conditions at $x = -x_p$ and $x = x_e$ are

$x = -x_p$

$$T_\mathrm{p} = T_\mathrm{g} = T_0, \quad Y_\mathrm{pro} = Y_\mathrm{soot} = 0, \quad q^+_{r,p}(-x_p) = \pi I_0 \tag{25}$$

$x = x_e$

$$\frac{\partial^2 T_\mathrm{g}}{\partial x^2} = 0, \quad \frac{\partial^2 Y_i}{\partial x^2} = 0, \quad q^-_{r,\mathrm{soot}}(x_e) = q^+_{r,\mathrm{soot}}(x_e). \tag{26}$$

4. Numerical method

The conservation equations for species and energy are transformed into dimensionless forms and approximated by finite-difference expressions. Table 1 lists the parameters used in the calculation [8,9,17,18]. The heat of the exothermic reaction, h_ex, was estimated from the temperature profile for the experiment at $\phi = 0.6$. As listed in Table 1, for soot formation, the reaction rate factors based on Tesner's model are slightly modified by fitting the calculated temperature profile and soot volume fraction to the measured ones. The reaction rate factor of radical oxidation was determined from the experimental result that the oxygen concentration is equal to 1% exhaust gas.

The initial soot particle diameter, d_p, was estimated from the critical soot particle diameter (10^{-9} m) at nucleation [19]. The molar mass, M_R, and density, ρ_R, of radicals in Eq. (12) are evaluated using the data of C_6H_6

Table 1
Parameters used in calculation

A_{ex} (s^{-1})	A_{en} ($kg^{-1}\,s^{-1}$)	h_{ex} (MJ/kg)	h_{en} (MJ/kg)	A_c (m^3/(kg s))	$f-g$ (s^{-1})	C_r	E_{ex} (kJ/mol)	E_{en} (kJ/mol)	a (s^{-1})	b (m^3/s)	g_0 (m^3/s)	l (m)
1.8×10^8	10^{34}	17	14	2.4×10^7	100	1.5	130	200	10^4	10^{-17}	10^{-6}	10^{-4}

which is considered to be the precursor of soot formation [8].

The calculated range of R_∞ is determined from the soot particle maximum radius when the accumulated soot volume fraction $f_{v,r}(r,x)=\int_{R_{\min}}^{r}\frac{4}{3}\pi p^3 N(r,x)\mathrm{d}p$ becomes constant. The coefficient C_r of Eq. (24) was estimated from both the mesh number and the calculation region, i.e., the maximum radius of the soot particles. The soot particle coalescence region (radius l) was determined by fitting the absorption coefficient, $\kappa_{soot}(x)$, and soot particle volume fraction, $f_{v,s}(x)$, to the corresponding measured values [7].

The energy balance obtained from the calculated results is satisfied within the accuracy of about 3%.

5. Results and discussion

5.1. Experimental results

Fig. 4(a)–(c) show profiles of the gas temperature, species concentration detected by TCD and FID, respectively, along the flow direction under the condition of the equivalence ratio of 2.6 and the mixture velocity of 2.4 cm/s, where the abscissas denote the distance from the downstream end of porous medium I. In Fig. 4(a), the solid line indicate the gas phase temperature estimated from the temperature (gray line) measured by the thermocouple. The mixture is preheated from the ambient temperature to approximately 900 K during the period when the gas flows through porous medium I. The gas temperature is drastically increased by exothermic reaction in the combustion space near porous medium I, and a luminous flame (yellow) is observed in the entire region of the downstream side of the exothermic reaction zone. At the end of this exothermic reaction zone, the oxygen concentration is almost equal to 1%. Many species, such as C_2H_2, C_3H_4 and C_6H_6, appear within this exothermic reaction zone. On the other hand, in the luminous flame zone (yellow zone), the gas temperature is sharply decreased along the flow direction. This is because a large amount of energy is transferred by radiation from the luminous flame to porous medium I; in the case of the luminous flame, the emissive power for thermal radiation is as strong as that of the porous radiative converter, and furthermore, the endothermic reaction for soot formation also occurs in this region.

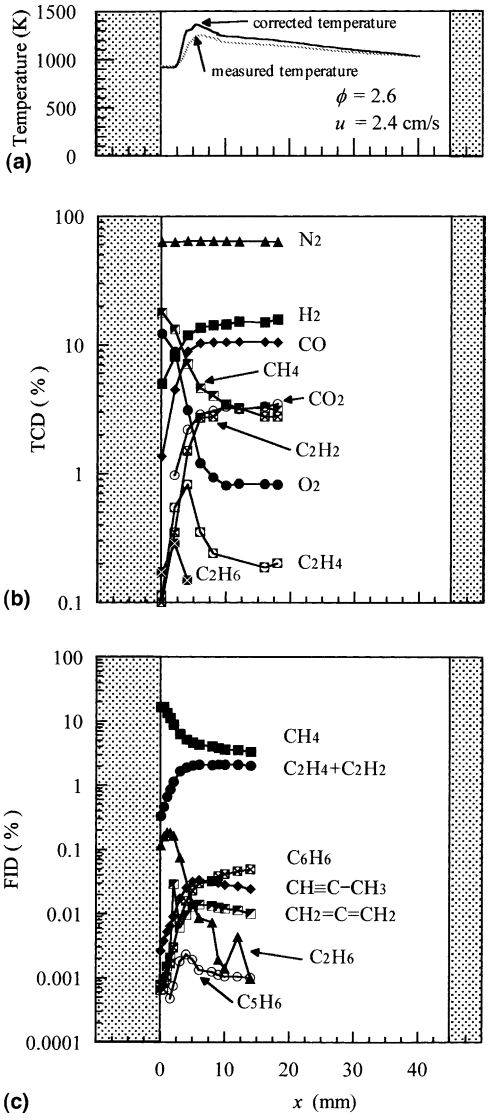

Fig. 4. (a) Temperature profiles. (b) Concentration profiles of species detected by TCD. (c) Concentration profiles of species detected by FID.

5.2. Modeling results

5.2.1. Flame temperature and species concentration

Fig. 5(a) and (b) show profiles of the gas temperature and species concentration of the flame, respectively. The

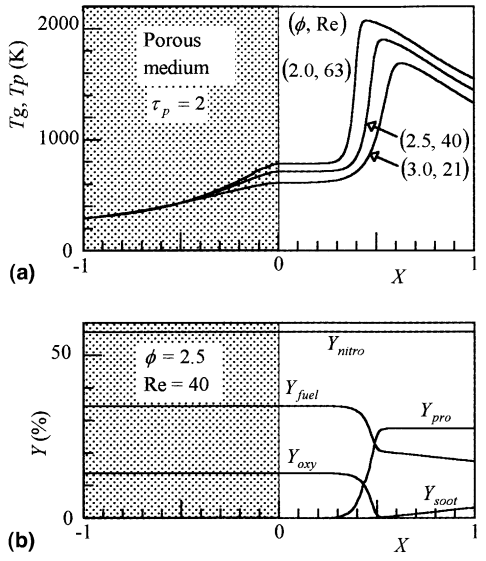

Fig. 5. (a) Calculated temperature profiles of flame. (b) Species concentration profiles.

X-axis is the dimensionless distance from the downstream end of the porous medium. The optical thickness for the porous medium, τ_p, the geometrical thickness for the porous medium, x_p, and the geometrical thickness for the combustion space, x_e, are 2, 50 and 50 mm, respectively. The inlet temperature of the mixture, T_0, is 298 K.

In order to clarify the difference for the equivalence ratio, the cases of $\phi = 2.0, 2.5$ and 3.0 are shown in Fig. 5(a). First, we consider the flame structure at $\phi = 2.5$ and $Re = 40$ as an example. The mixture is preheated in the porous medium, and the flame is stabilized in the downstream side of the porous medium. The gas temperature, T_g, reaches a maximum when the oxygen concentration, Y_{oxy}, is nearly equal to zero. After the exothermic reaction, the endothermic reaction for soot formation takes place. The soot concentration, Y_{soot}, increases along the flow direction. On the other hand, the gas temperature, T_g, and the fuel concentration, Y_{fuel}, decrease, and the products concentration, Y_{pro}, becomes constant in this region. These flame structures are basically common to the cases for other equivalence ratios.

As shown in Fig. 5(a), the flames are stabilized far from the porous medium under super fuel-rich conditions, as a result of the total heat balance between the combustion heat and the heat transferred to the upstream side porous medium. This flame behavior is quite similar to that observed through the experimental measurements, as shown in Fig. 4(a). Furthermore, it is clarified that the distributions of the fuel and the products mole fractions, Y_{fuel} and Y_{pro} in Fig. 5(b), are respectively much similar to those of the CH_4 mole fraction and the sum of the H_2, CO, CO_2 and C_2H_2 mole fractions in Fig. 4(b), because the intermediate species mole fractions are very small. Consequently, the numerical model introduced here is quite reasonable for the expression of the soot formation.

5.2.2. Soot particle growth process

Fig. 6 shows (a) radical number density $n_R(X)$, (b) soot number density $N_s(x)$, (c) soot volume fraction $f_{v,s}(X)$, (d) absorption coefficient of soot $\kappa_{soot}(X)$, and (e) mean soot particle radius $r_{ave}(X)$. In order to clarify the effect of the equivalence ratio, the profiles of the cases of $\phi = 2.0$ ($Re = 63$), 2.5 ($Re = 40$) and 3.0 ($Re = 21$) are shown in Fig. 6(a)–(e). The soot number density $N_s(x)$ and mean soot particle radius $r_{ave}(X)$ are expressed as

$$N_s(x) = \int_{R_{min}}^{R_\infty} N(r,x)\,dr \tag{27}$$

$$r_{ave}(X) = \sqrt[3]{\frac{3}{4\pi}\frac{f_{v,s}(X)}{\int_{R_{min}}^{R_\infty} N(r,X)\,dr}}. \tag{28}$$

Since the results do not differ significantly for various equivalence ratios, we consider the results for $\phi = 2.5$ and $Re = 40$ as an example. As shown in Fig. 5(a), the gas temperature reaches a maximum at $X = 0.53$, and in Fig. 6(a) the radical number density reaches a maximum at $X = 0.54$; thus, the radical number density n_R initially increases owing to the high gas temperature T_g and high fuel concentration Y_{fuel}. The radical number density n_R, however, decreases with decreasing gas temperature T_g and increasing soot number density $N_s(X)$; that is, the soot number density $N_s(X)$ abruptly increases with increasing radical number density n_R and reaches a maximum at $X = 0.59$. The soot volume fraction $f_{v,s}(X)$, the absorption coefficient of soot particles $\kappa_{soot}(X)$ and the mean soot particle radius $r_{ave}(X)$ increase along the flow direction.

In order to clarify the soot particle growth process, Fig. 7(a) and (b) show the distribution of soot number density $N(r,X)$ along the flow direction. In Fig. 7(a), the initial soot number density increases in association with the formation of radicals in the downstream side (from $X = 0.5$ to 0.6) of the maximum gas temperature. Along the flow direction, the soot number density $N(r,X)$ for smaller particle size decreases as shown in Fig. 7(b), but that for larger particle size increases as shown in Fig. 7(a). Fig. 7(c)–(f) show the local soot number density balance at $X = 0.5$ and 0.8. Fig. 7(g) shows the growth rate of the soot particle surface area. The substantial growth rate of the soot particle surface area $s'_a(r,x)$ indicated by solid lines in Fig. 7(g), and the surface growth rate of soot particle area $s'_e(r,x)$ indicated by gray lines in Fig. 7(g), are expressed as

$$s'_a(r,x) = 4\pi[(r + r'_a(r,X)\,dx/u)^2 - r^2]/(dx/u) \tag{29}$$

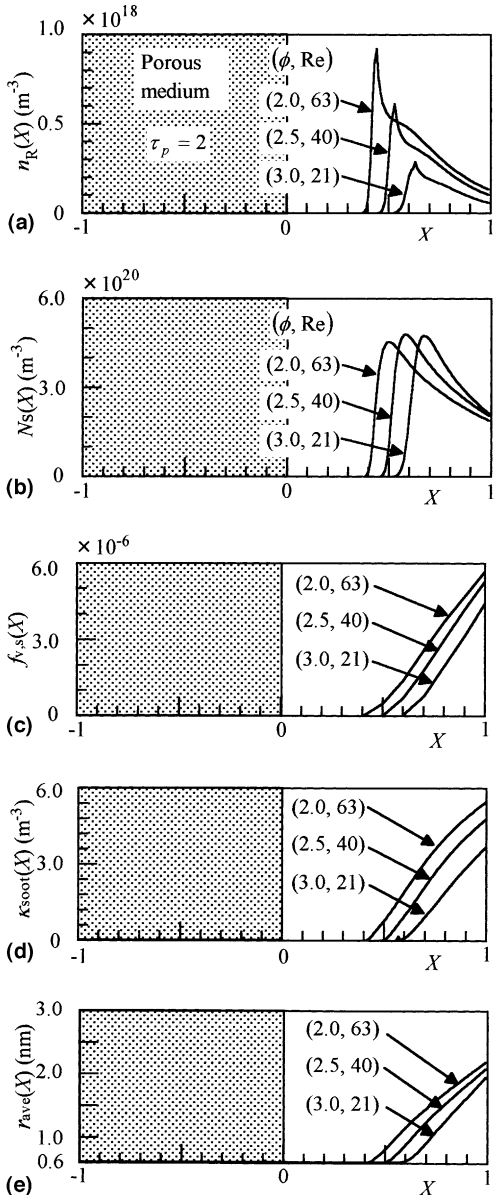

Fig. 6. (a) Profiles of radical number density. (b) Profiles of soot particle number density. (c) Profiles of soot volume fraction. (d) Profiles of absorption coefficient of soot. (e) Profiles of mean soot particle radius.

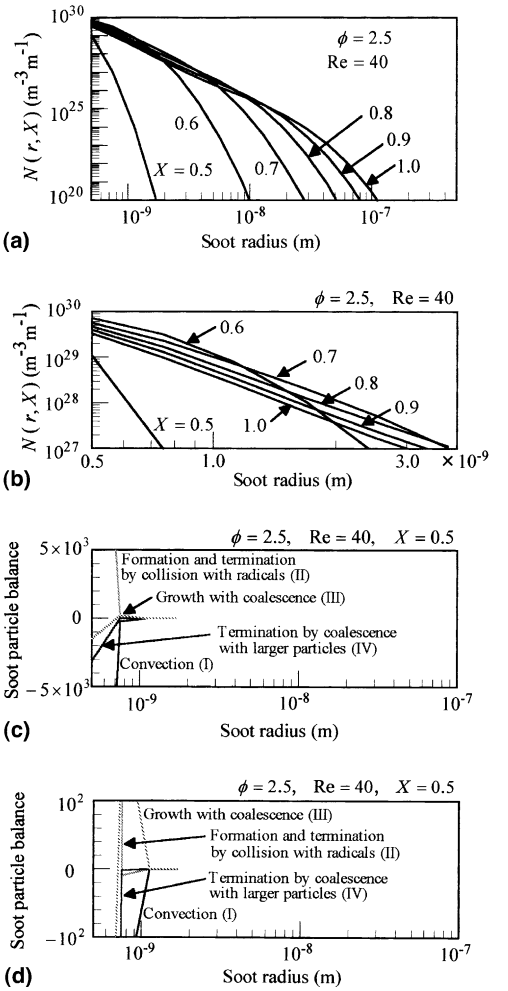

Fig. 7. (a) Distribution of soot particle number density along the flow direction. (b) Distribution of soot particle number density along the flow direction. (c) Local soot particle number density balance ($X = 0.5$). (d) Local soot particle number density balance ($X = 0.5$). (e) Local soot particle number density balance ($X = 0.8$). (f) Local soot particle number density balance ($X = 0.8$). (g) Growth rate of soot particle surface area along the flow direction. (h) Local soot volume fraction and accumulated soot volume fraction.

$$s'_e(r,x) = 4\pi[(r + r'_e(r,X)\,\mathrm{d}x/u)^2 - r^2]/(\mathrm{d}x/u). \qquad (30)$$

As seen in Fig. 7(c), at $X = 0.5$, the initial soot particles mainly flow out by convection (I), and decrease owing to the surface–coalescence growth of smaller soot particles (III) and coalescence with larger soot particles (IV). In Fig. 7(d), in the case of soot particles whose radii sare larger than 0.8 nm, soot particles grow by surface–coalescence growth of smaller soot particles (III), and mainly flow out by convection (I). At $X = 0.5$, the surface growth $s'_e(r,x)$ is considered to be the principal cause of soot growth, because in Fig. 7(g) $s'_e(r,x)$ indicated by dotted lines at $X = 0.5$ and at $X = 0.9$ are overlapped. When $X > 0.5$, the surface growth $s'_e(r,x)$ becomes dominant for small soot particles, while the coalescence growth becomes dominant for large soot particles.

In Fig. 7(e), at $X = 0.8$, in the case of soot particles whose radii are smaller than 5 nm, the soot number density increases owing to conversion (I) and surface–coalescence growth with smaller soot particles (III), and

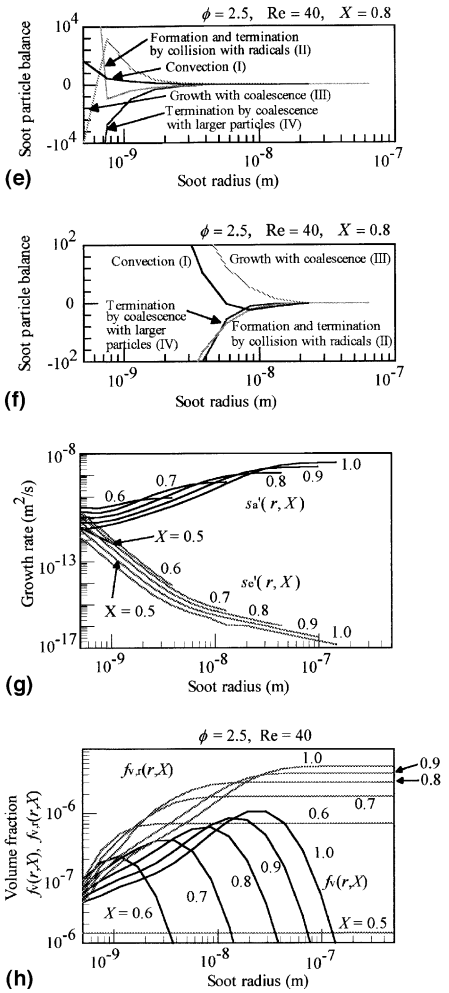

Fig. 7 (*continued*)

decreases owing to the collision with radicals (II) and the coalescence with larger soot particles (IV). In Fig. 7(f), for soot particles whose radii are larger than 5 nm, the soot number density increases owing to surface–coalescence growth with smaller soot particles (III), and decreases owing to convection (I), coalescence with larger soot particles (IV), and collision with radicals (II).

Fig. 7(h) shows the local soot volume fraction $f_v(r,X)$ and accumulated soot volume fraction $f_{v,r}(r,X)$ indicated by a gray line. In the local soot volume fraction $f_v(r,X)$ distribution shown in Fig. 7(h), the peak shifts from $r = 1$ nm to 30 nm. The accumulated soot volume fraction $f_{v,r}(r,X)$ becomes almost constant in the region of $r > 100$ nm. Therefore, the soot particle diameter is considered to reach approximately 100 nm in the downstream side. The order of these values corresponds to those for the CH_4-O_2 flame [19], i.e., mean soot particle radius of 5–80 nm, total soot volume fraction of 10^{-8}–10^{-5}, and those to spectroscopical

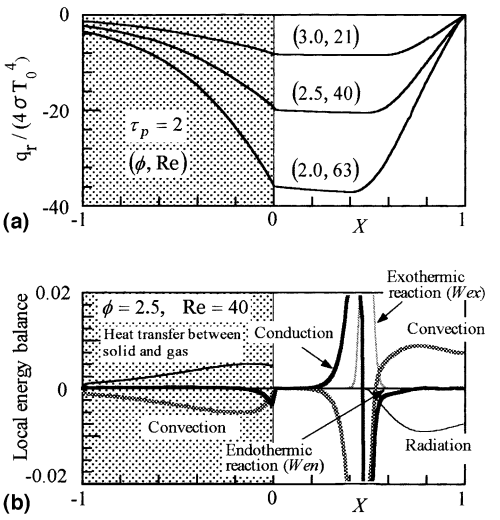

Fig. 8. (a) Profiles of nondimensional net radiation flux. (b) Local energy balance of gas phase.

measurement [7], i.e., mean soot particle radius of 70 nm, total soot volume fraction of 10^{-7}, and the absorption coefficient for luminous flame of 2 m^{-1}.

5.2.3. Flame structure

Fig. 8(a) and (b) show the profiles of the net radiation flux and local energy balance, respectively. The flowing gas enthalpy is effectively converted into radiant energy via the soot particles. Radiant energy is absorption by the upstream porous medium in which the mixture is preheated. Therefore, the fuel-rich premixed flame for the equivalence ratio above the flammability limit is sustained due to heat recirculation through radiation. Soot particles play the role of porous radiative converters in the combustion space.

6. Conclusions

In the present study, the soot particle growth process and the flame structure of the fuel-rich premixed flame have been investigated by means of a one-dimensional numerical analysis. A novel model for soot formation has been developed by taking coalescence and surface growth into account; the coalescence probability is statistically evaluated for polydispersed soot particles. Although actual soot particles grow with a chain-like structure, the present model which treats soot particles as spheres is considered to demonstrate qualitatively correct features. The conclusions are as follows:

1. In the vicinity of the soot inception region, soot particles mainly increase due to the surface growth and decrease as a result of convection.

2. In the downstream side, small soot particles increase due to convection and grow by coalescence with smaller soot particles, and decrease as a result of collision with radicals and coalescence with larger soot particles.

On the other hand, large soot particles grow by coalescence, and decrease due to convection, coalescence with larger soot particles and collision with radicals.

Acknowledgements

This work was supported in the part by the Ministry of Education, Culture, Sports, Science and Technology under Grants-in-Aid for Science Research(A) (no. 01420023) and for the Encouragement of Young Scientists (no. 06750192).

References

[1] R. Echigo, H. Yoshida, K. Hanamura, M. Okuyama, T. Koganezawa, K. Hijikata, A new approach to reduce CO_2 emission by radiation-controlled combustion and carbon recovery, in: Proceedings of Third ASME/JSME Thermal Engineering Joint Conference, vol. 3, 1991, pp. 257–263.

[2] S.B. Haynes, H. Jander, H. Matzing, H. GG. Wagner, The influence of gaseous additives on the formation of soot in premixed flames, in: 19th International Symposium on Combustion, 1982, pp. 1379–1385.

[3] F. Mauss, T. Schafer, H. Bockhorn, Inception and growth of soot particles in dependence on the surrounding gas phase, Combust. Flame 99 (1994) 697–705.

[4] F.D. Lai, K.S. Friedlander, J. Pich, G.M. Hidy, The self-preserving particle size distribution for Brownian coagulation in the free-molecule regime, J. Colloid Interface Sci. 39 (2) (1972) 395–405.

[5] R. Echigo, Radiation enhanced/controlled phenomena of heat and mass transfer in porous media, in: Proceedings of Third ASME/JSME Thermal Engineering Joint Conference, vol. 4, 1991, pp. 21–32.

[6] R. Echigo, Exergy regenerating combustion for advanced energy conversion, in: Proceedings of Third KSME/JSME Thermal Engineering Joint Conference, vol. 3, 1996, pp. 1–8.

[7] M. Okuyama, R. Echigo, H. Yoshida, M. Koda, K. Hanamura, Spectral radiation properties of super fuel-rich premixed flame, Transport Phenomena in Combustion, vol.2, Taylor& Francis, 1995, pp. 1795–1806.

[8] M. Okuyama, T. Koganezawa, K. Hanamura, R. Echigo, H. Yoshida, Reaction mechanism of super fuel-rich premixed flame controlled by radiation, Trans. JSME B 62 (598) (1996) 2490–2497 (in Japanese).

[9] M. Okuyama, K. Hanamura, R. Echigo, H. Yoshida, Structure of super fuel-rich premixed flame, Transport Phenomena in Combustion, vol. 1, Taylor & Francis, 1995, pp. 275–285.

[10] P.A. Tesner, T.D. Snegiriova, V.G. Knorre, Kinetics of dispersed carbon formation, Combust. Flame 17 (1970) 253–260.

[11] H. Bockhorn, F. Fetting, G. Wannemacher, H.W. Wenz, Optical studies of soot particle growth in hydrocarbon oxygen flames, in: Nineteenth International Symposium on Combustion, 1982, pp. 1413–1420.

[12] H. Tanaka, A theoretical study of dropwise condensation, Trans. ASME, Heat Transfer 97 (1975) 72–78.

[13] H. GG. Wagner, Soot formation in combustion, in: Seventeenth International Symposium on Combustion, 1978, pp. 3–19.

[14] Y. Yoshizawa, K. Sasaki, R. Echigo, Analytical study of the structure of radiation controlled flame, Int. J. Heat Mass Transfer 31 (2) (1988) 311–319.

[15] W.W. Yuen, C.L. Tien, A simple calculation scheme for the luminous-flame emissivity, in: Sixteenth International Symposium on Combustion, 1976, pp. 1481–1478.

[16] W.H. Dalzell, A.F. Sarofim, Optical constants of soot and their application to heat-flux calculations, Trans. ASME, Heat Transfer 91 (1969) 100–105.

[17] K. Hanamura, Y. Yoshizawa, R. Echigo, Analytical study on the structure of radiation controlled flame, Trans. JSME B 56 (529) (1990) 268–274 (in Japanese).

[18] K. Hanamura, R. Echigo, Y. Yoshizawa, Structure and transient behavior of radiation-controlled flame in a highly porous medium, Trans. JSME B 57 (533) (1991) 315–321 (in Japanese).

[19] A. D'allesio, A. DI. Lorenzo, A.F. Sarofim, F. Beretta, S. Masi, C. Ventitozzi, Soot formation in methane-oxygen flames, in: Fifteenth International Symposium on Combustion, 1975, pp. 1427–1437.